University of South Florida
Digital Commons @ University of South Florida

DIGITAL COMMONS
@ UNIVERSITY OF SOUTH FLORIDA

Marine Science Faculty Publications | College of Marine Science

5-15-2001

Equatorial Upwelling in the Western Pacific Warm Pool

Robert W. Helber
University of South Florida

Robert H. Weisberg
University of South Florida, weisberg@marine.usf.edu

Follow this and additional works at: https://digitalcommons.usf.edu/msc_facpub

 Part of the Marine Biology Commons

Scholar Commons Citation

Helber, Robert W. and Weisberg, Robert H., "Equatorial Upwelling in the Western Pacific Warm Pool" (2001). *Marine Science Faculty Publications*. 128.
https://digitalcommons.usf.edu/msc_facpub/128

This Article is brought to you for free and open access by the College of Marine Science at Digital Commons @ University of South Florida. It has been accepted for inclusion in Marine Science Faculty Publications by an authorized administrator of Digital Commons @ University of South Florida. For more information, please contact digitalcommons@usf.edu.

JOURNAL OF GEOPHYSICAL RESEARCH, VOL. 106, NO. C5, PAGES 8989–9003, MAY 15, 2001

Equatorial upwelling in the western Pacific warm pool

Robert W. Helber and Robert H. Weisberg
Department of Marine Science, University of South Florida, St. Petersburg, Florida

Abstract. Vertical velocity on the equator in the western Pacific warm pool is investigated using data from the Coupled Ocean-Atmosphere Response Experiment enhanced monitoring array (EMA) centered at 0°, 156°E. The data consist of hourly subsurface horizontal velocity time series from August 1991 until April 1994. Vertical velocity is calculated using horizontal velocity components and the application of the continuity equation. During the first year, from March 1992 until February 1993, data are available from five moorings of the EMA and thus provide nine different combinations of moorings from which to calculate vertical velocity. Four moorings were available during the remaining time period. Random errors are found to be $<10^{-5}$ m s^{-1}, while systematic errors (finite difference error, systematic instrument error, and error due to surface extrapolation) may be larger. It is suggested that errors, including finite difference errors, are not larger than the vertical velocity estimate. The estimates of vertical velocity are valid on spatial scales the size of the array (~400 km) and timescales longer than a few days. They reveal a seasonal cycle manifested during a moderate El Niño. Results indicate upwelling, on average from 70 m down to 250 m over the 2 year time period, being slightly stronger in 1992 coincident with the stronger El Niño year. The divergence of horizontal velocity components, resulting in positive vertical velocity, is due to geostrophic divergence on the equator produced from a westward directed zonal pressure gradient force. Meridional divergence and zonal wind stress are uncorrelated, suggesting that Ekman convergence due to local westerly winds is only of partial influence. Consequently, downwelling is not found near the surface, where contributions from local winds and geostrophic divergence are in opposition. This estimate of vertical velocity indicates that water is upwelled in the warm pool from much deeper than but with comparable magnitude to the central and eastern Pacific.

1. Introduction

Equatorial upwelling results from the competing influences of Ekman and geostrophic flows [e.g., *Wyrtki*, 1981]. Where the easterly trade winds prevail in the equatorial eastern and central Atlantic and Pacific Oceans, Ekman divergence and geostrophic convergence produce upwelling above the Equatorial Undercurrent (EUC) with downwelling below [e.g., *Wyrtki and Kilonsky*, 1984; *Bryden and Brady*, 1985; *Weingartner and Weisberg*, 1991; *Qiao and Weisberg*, 1997; *Weisberg and Qiao*, 2000]. This is a consequence of the scale mismatch between the near-surface Ekman divergence and the zonal pressure gradient–induced geostrophic convergence that penetrates deeper.

In other equatorial regions, where the prevailing easterly trade winds are not present, equatorial upwelling is poorly understood. In this article we describe equatorial upwelling in the western Pacific warm pool, where winds are generally light and where during El Niño phases of El Niño–Southern Oscillation (ENSO), large episodic westerly wind bursts occur. The seasonal occurrence of these strong westerly wind bursts within a relatively calm region results in a pattern of reversing zonal currents that produce contrasting seasons with different vertical structure. A transition occurs when the entire eastward flowing water column, down to at least 260 m, is followed by a season where there is westward flow sandwiched between an eastward surface current and the eastward flowing EUC [*Cronin et al.*, 2000]. Equatorial upwelling in the warm pool is therefore expected to be different from that in the central and eastern Pacific and the Atlantic.

Moored subsurface acoustic Doppler current profilers (ADCPs) were deployed as part of the Coupled Ocean-Atmosphere Response Experiment (COARE) enhanced monitoring array (EMA) in the western Pacific warm pool centered at 0°, 156°E. The array consisted of five moorings that recorded horizontal velocities down to 260 m. Vertical velocity is obtained using the continuity equation by vertically integrating horizontal divergence calculated via finite differencing [e.g., *Bubnov*, 1987; *Halpern and Freitag*, 1987; *Halpern et al.*, 1989; *Weingartner and Weisberg*, 1991; *Johnson and Luther*, 1994; *Qiao and Weisberg*, 1997; *Weisberg and Qiao*, 2000]. An indirect method of estimating vertical velocity is required since values of vertical velocity, even in regions of strong equatorial upwelling, are only of the order 10^{-5} m s^{-1}. The use of moored ADCP measurements in the present analysis provides time-depth coverage of vertical velocity from February 1992 until April 1994 from the surface to 250 m depth.

2. Field Program, Data, and Methods

2.1. COARE Enhanced Monitoring Array

During the COARE Intensive Observing Period (IOP) an extensive observational network was positioned near 2°S, 156°E [*Godfrey et al.*, 1998]. The purpose of the EMA was to set the IOP observations within the context of the larger-scale

Copyright 2001 by the American Geophysical Union.

Paper number 2000JC000401.
0148-0227/01/2000JC000401$09.00

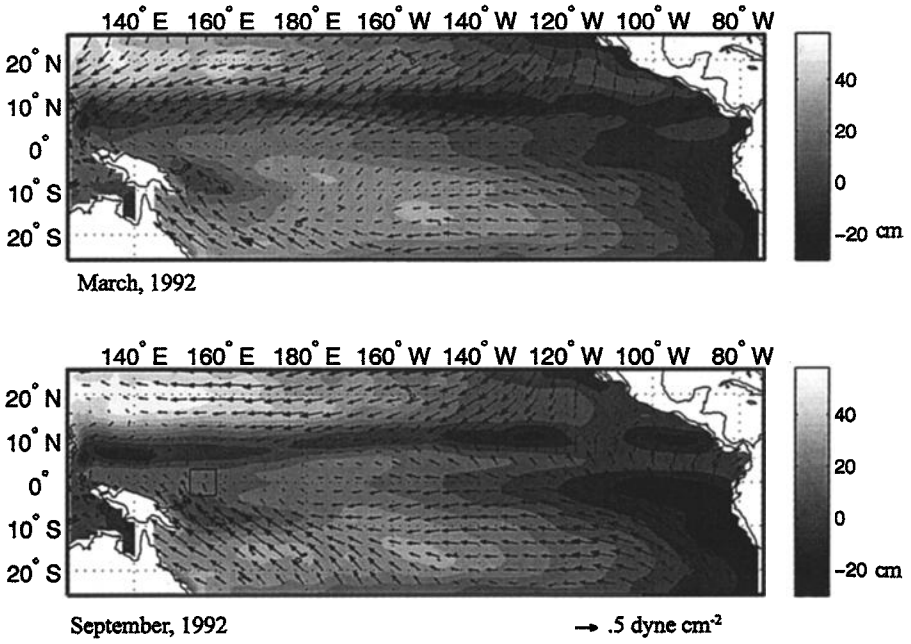

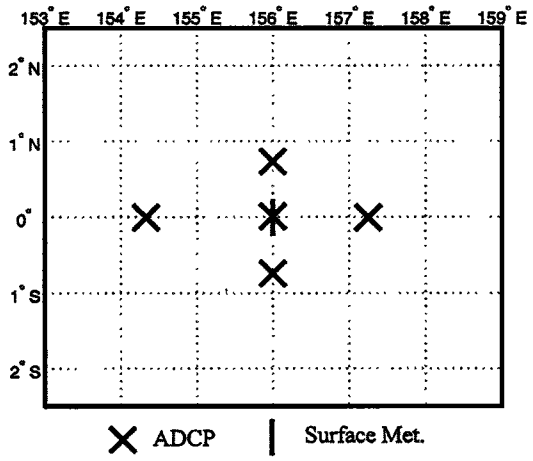

Figure 1. The portion of the COARE EMA relative to Leetmaa Pacific Ocean Reanalysis surface pressure and winds stress monthly averages for March and September 1992. Surface pressure is in cm, and wind stress is in dyne cm^{-2}. See Table 1 for data coverage details.

variability. A portion of the EMA (Figure 1) was centered at 0°, 156°E, lasted from August 1991 until April 1994, and was deployed within the pre-existing Tropical Atmosphere-Ocean (TAO) array.

Our analysis primarily uses moorings that were located at 0°, 154°E; 0°, 156°E; 0°, 157°30′E; 0°45′N, 156°E; and 0°45′S, 156°E. Subsurface horizontal velocity time series at these moorings were profiled hourly from depths as shallow as 10 m down to 260 m [*Weisberg et al.*, 1993, 1994; *Kutsuwada and Inaba*, 1995; *Cronin et al.*, 2000] (see Figure 1 and Table 1).

Surface meteorological and subsurface temperature and salinity data, which were also part of the EMA, are used for diagnosing the forcing components responsible for vertical velocity. *Cronin and McPhaden* [1997] computed wind stress using surface meteorological data from the mooring located at 0°, 156°E with the use of the COARE v2.5b bulk flux algorithm. In addition, *Cronin et al.* [2000] derived dynamic height referenced to 500 m using subsurface temperature and salinity data from TAO moorings located at 0°, 154°E; 0°, 156°E; 0°, 160.5°E; and 0°, 165°E. These data are used to analyze the zonal momentum on the equator.

To provide a larger-scale representation of the zonal pressure gradient force and wind field, Leetmaa Pacific Ocean Reanalysis [*Leetmaa and Ji*, 1989] fields were obtained from the Climate Diagnostic Center. The surface pressure and wind stress for March and September 1992 in the tropical Pacific are shown in Figure 1.

2.2. Horizontal Velocity Components

Various descriptions of the data used in this analysis are given by *Kutsuwada and Inaba* [1995], *Helber and Weisberg* [1998], *Cronin et al.* [2000], and R. W. Helber et al. (Upper

Table 1. Temporal and Spatial Coverage of the Enhanced Monitoring Array Acoustic Doppler Current Profiler Data[a]

Location	Dates	Top Bin, m	Bottom Bin, m	Sample Rate
0°, 154°E	Nov. 6, 1992, to Feb. 16, 1993	30	240	hourly
0°, 154°E	March 1, 1992, to Feb. 15, 1993	30	240	daily
0°, 156°E	Aug. 29, 1991, to March 8, 1993	10[b]	255	hourly
0°, 156°E	March 12, 1993, to April 27, 1994	30	260	hourly
0°, 157.5°E	Feb. 11, 1992, to April 4, 1994	30	260	hourly
0.75°N, 156°E	Feb. 11, 1992, to April 4, 1994	30	260	hourly
0.75°S, 156°E	Feb. 11, 1992, to April 3, 1994	30	260	hourly

[a] With a sampling increment of 10 m the top and bottom bins are the upper and lower sampling depths after initial data editing procedures, respectively.

[b] The 10 m top bin was available only when the ADCP was downward looking from August 28, 1991, until March 3, 1993. The rest of the time the ADCP was upward looking, and the top bin was at 30 m. At all other locations the ADCPs were upward looking.

ocean thermodynamics on the equator in the western Pacific warm pool, submitted to *Journal of Geophysical Research*, 2000). To highlight features of the data relevant to the vertical velocity estimation, contour plots of the horizontal velocity components (denoted u and v, corresponding to eastward and northward in the x and y coordinate directions, respectively) are shown in Figure 2. For display purposes the data are low-pass filtered to exclude timescales shorter than 25 days.

The 2-year long subsurface horizontal velocity observations reveal what appears to be a seasonal cycle, which is also present in vertical velocity. The zonal current structure is characterized by a 2 or 3 month season in boreal summer when the entire upper ocean is flowing eastward. Starting in August, during this eastward flow the EUC begins a deceleration that lasts for several months. In September, while the EUC is decelerating, there is an abrupt onset of westward flow from the surface to 150 m. This transition, characterized by the onset of the subsurface westward flow, delineates two dynamic realms that are also apparent in the vertical velocity estimation. All of these features appear at all moorings of the EMA during both years and represent large-scale features relative to the array.

Because of the variable nature of the surface flow and the seasonally occurring subsurface westward flow, the u component record length mean is near zero at 100 m and above. Below 100 m the influence of the EUC on the mean u profile dominates (Figure 2). On average, the v component is weakly southward, <0.1 m s^{-1}, near the surface and from 90 to 200 m. Near the average depth of the thermocline top, ~70 m, the mean v component is zero.

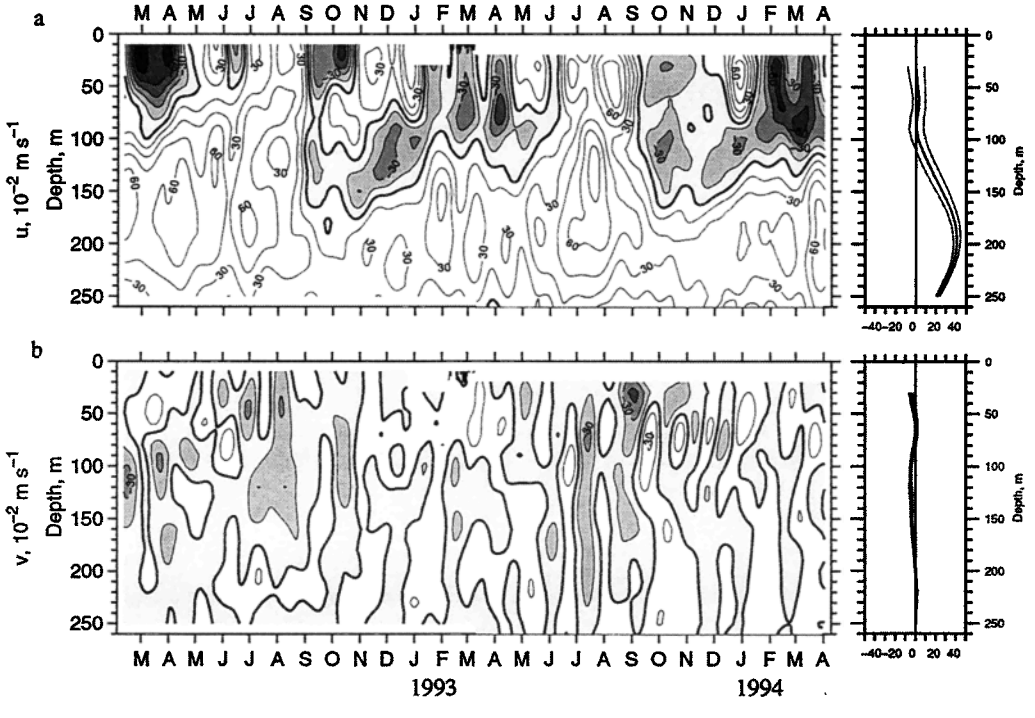

Figure 2. Horizontal velocity from the mooring located at 0°, 156°E from February 10, 1992, until April 4, 1994. Time-depth contours of (a) eastward and (b) northward subsurface velocity are in units of 10^{-2} m s^{-1} with a contour interval of 15×10^{-2} m s^{-1}. To the right of the time-depth contours is the corresponding record length mean (heavy line) with plus and minus the standard deviation of the mean (thin lines) versus depth. Data are filtered to remove oscillations of period 25 days or less.

2.3. Vertical Velocity

The divergence of the vertical velocity component (denoted w and positive upward in the z coordinate direction) is obtained from the divergence of horizontal velocity components using the continuity equation

$$\frac{\partial w}{\partial z} = -\left[\frac{\partial u}{\partial x} + \frac{\partial v}{\partial y}\right].$$

With the condition that w is zero at the surface, integration in z produces w as a function of depth.

When performing this calculation using data from a mooring array, additional assumptions arise out of necessity. Because finite differences are used for $\partial u/\partial x$ and $\partial v/\partial y$, the control volume, implicitly assumed by the continuity equation, becomes defined by the spacing between the data points. In this situation the largest zonal and meridional dimensions of the control volume are 389 and 167 km, respectively, depending on the combination of the moorings used. Since the data are in 10 m depth bins, the vertical dimension of the control volume is 10 m. The horizontal divergence obtained at each sampling depth is then integrated in z using the trapezoidal method. Under the conditions of this method, w is obtained accurately, with minimal finite difference error, when the curvature in the spatial variability of the horizontal currents is small relative to the size of the array and the depth sampling interval. The relatively small vertical sampling interval combined with the use of the trapezoidal integration method minimizes finite difference error in the vertical. The finite difference error due to the horizontal size of the array, however, may be large and is discussed in section 2.4.2.

The five moorings result in three different estimates of both $\partial u/\partial x$ and $\partial v/\partial y$, producing nine different estimates of w, which we refer to as phases one through nine. We call them phases because an effect of varying the finite differences is to shift the estimated phase of a wave that propagates past the array. Figure 3 identifies the phase numbering convention. Since phase five w estimation uses center differences for both $\partial u/\partial x$ and $\partial v/\partial y$, the phase of a passing wave is estimated without shift. Phase six w would estimate the phase of a passing wave shifted zonally in one direction, while phase four would estimate the phase of the same passing wave shifted zonally in the other direction. In addition to being the estimate of w without phase shift, phase five is also the largest-scale estimate from the array being identical to the average of all nine estimates.

Figure 4 shows the resulting w from the nine combinations of divergence calculations. Present in all nine estimates is a bimodal character of w. In boreal summer, months June, July, and August, there is upwelling in each phase. After the onset of the subsurface westward flow in September, w is more variable and primarily negative.

The average vertical velocity profiles, shown in Figure 5, show a profile that can vary in magnitude, from phase to phase, particularly with the deeper values below 175 m, by as much as 5×10^{-5} m s^{-1}. The vertical velocity profile, being positive over most of the upper ocean water column, is consistent with a westerly wind–driven geostrophic divergence but does not account for the convergence expected from the surface Ekman transport also due to the westerly winds. Above 75 m, w is not substantially different from zero in most phases. Westerly winds, though not constant, prevail over the averaging time period with a mean of 0.7 m s^{-1} (see Figure 12). In the presence of these winds it is surprising not to find downwelling. Upwelling due to geostrophic divergence apparently cancels Ekman convergence and downwelling.

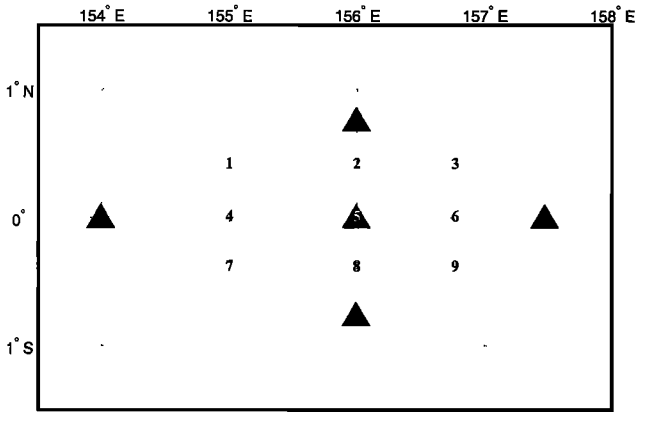

Figure 3. The numbering convention used to identify the phases of the vertical velocity estimation. Triangles mark the locations of the horizontal velocity moorings. The first row of numbers (1, 2, and 3) represents phases that calculate meridional divergence $\partial v/\partial y$ using moorings located at 0.75°N, 156°E and 0°, 156°E. The second row uses moorings at 0.75°N, 156°E and 0.75°S, 156°E for meridional divergence, while the third row uses moorings at 0°, 156°E and 0.75°S, 156°E. The first column of numbers (1, 4, and 7) represents phases that calculate zonal divergence $\partial u/\partial x$ using moorings located at 0°, 156°E and 0°, 154°E. The second column uses moorings at 0°, 157.5°E and 0°, 154°E for zonal divergence, while the third column uses moorings at 0°, 157.5°E and 0°, 156°E.

2.4. Error Analysis

2.4.1. Random error. There are two types of random errors inherent in the w estimation. The first type is due to the ADCPs' error of ~0.02 m s^{-1} for each hourly ensemble average and the mooring positions error of ~0.02°. Using standard propagation of error [i.e., *Beers*, 1957; *Chatfield*, 1978], these error sources in w grow with depth amounting to $<9 \times 10^{-6}$ m s^{-1} at 260 m for the estimate filtered to remove oscillations with a period of 5 days or less. A longer-period filter reduces this error since the number of ensembles averaged together increases with increased filter period. This is not a substantial error compared to the systematic errors discussed in section 2.4.2.

The second type of random error is due to the fact that geophysical time series are modulated over the timescales of interest. Consequently, any averaging in the experimental method has an inherent random error even in the event of perfect instruments. This error is the inherent geophysical random error, which depends on the record length relative to the intrinsic bandwidth of the time series. Since this error is not fully quantifiable, we are left with the caveat that this experiment done at some other time would produce different results. Where possible, we will identify known deviations by longer timescale variability such as ENSO.

When calculating averages as in Figures 2, 5, 6, 7, and 12, the standard deviation of the mean is obtained by dividing the standard deviation of the time series by the square root of the number of degrees of freedom [e.g., *Parratt*, 1961]. In all cases the number of degrees of freedom, calculated from the integral of the correlation function (integral timescale), and the stan-

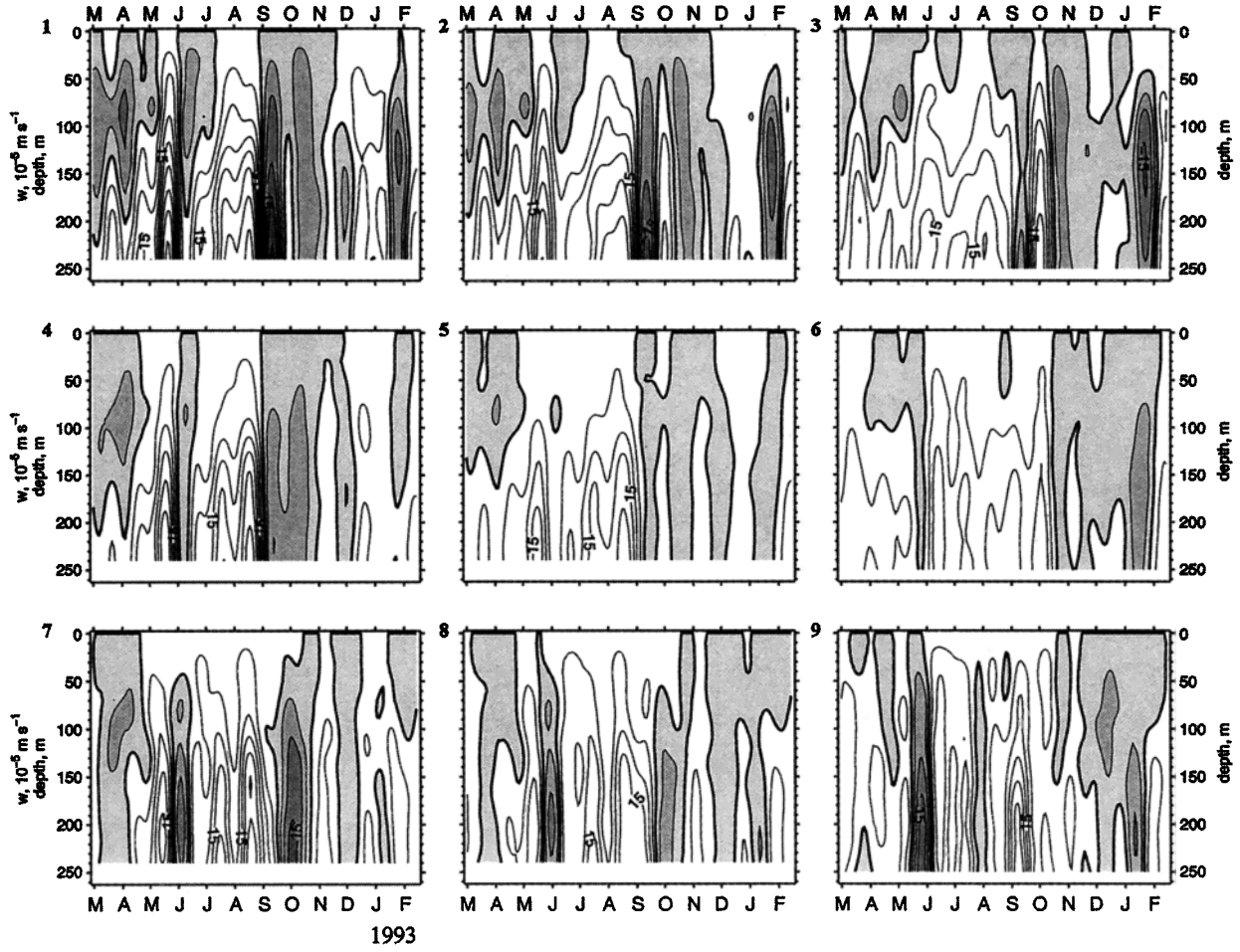

Figure 4. Time-depth contours of the nine phases of the vertical velocity estimation during the first year of data, from March 1, 1992, until February 15, 1993. The units are 10^{-5} m s^{-1}, the contour interval is 5×10^{-5} m s^{-1}, and the number in the upper left-hand corner of each panel corresponds to the numbering convention used in the text and shown in Figure 3. All data are filtered to remove oscillations of period 25 days or less.

dard deviation of the time series are determined at every depth. These random error determinations are separate from the systematic errors.

2.4.2. Systematic errors. The dominant errors in the w estimation are systematic and come from three sources: systematic instrument error, surface extrapolation error, and finite difference error. Systematic instrument errors are due to compass calibration, which, for the ADCPs used, is specified by the manufacturer to be accurate to within 2°. To quantify how large this error could become in the vertical velocity estimate, we have performed a worst case scenario using phase five w estimation. Horizontal velocity vectors from the four moorings used in phase five w were rotated by 2° such that the velocity vector from the 0°, 157.5°E mooring was rotated clockwise 2° while the velocity vector from the 0°, 154°E mooring was rotated counterclockwise 2°. In this way the compass error produced in $\partial u/\partial x$ would accumulate in the worst possible way (Figure 6b). The same alternating rotation was used for the moorings used in $\partial v/\partial y$. A similar analysis was performed on an estimate of w from horizontal ADCP velocity data at 0°, 140°W in the Pacific Ocean [*Weisberg and Qiao*, 2000] during the Tropical Instability Wave Experiment (TIWE). Since compass error grows with depth, the largest possible error was estimated, at the TIWE array, to be nearly two thirds of the vertical velocity value at 250 m. The present analysis reveals smaller compass error for this experiment presumably because of the weaker zonal currents in the warm pool. The largest compass error is found when the zonal velocity is greatest from April until September 1992 coinciding with the time period when the horizontal velocity components are strongest, most divergent, and produce upwelling.

Surface extrapolation error is due to side lobe reflection, which, for the upward looking ADCPs of this experiment, make velocity measurements above 30 m unavailable. Because in the calculation of w the horizontal divergence had to be connected with the boundary condition at the surface ($w = 0$), these near-surface velocity values were estimated by extrapolation. Since the center mooring, located at 0°, 156°E, had a downward looking ADCP during the EMA IOP, velocity data as shallow as 10 m were available (Table 1). The near-surface measurements from this mooring were used to estimate the magnitude of the extrapolation error. This error was smallest when the velocity profiles were extrapolated as a constant from the shallowest bin (see Table 1) to the surface.

Surface extrapolation error was taken as the square root of the difference of the squares of measured (when available) and constant extrapolated near-surface values. When measured values are not available, the error was taken as the square root

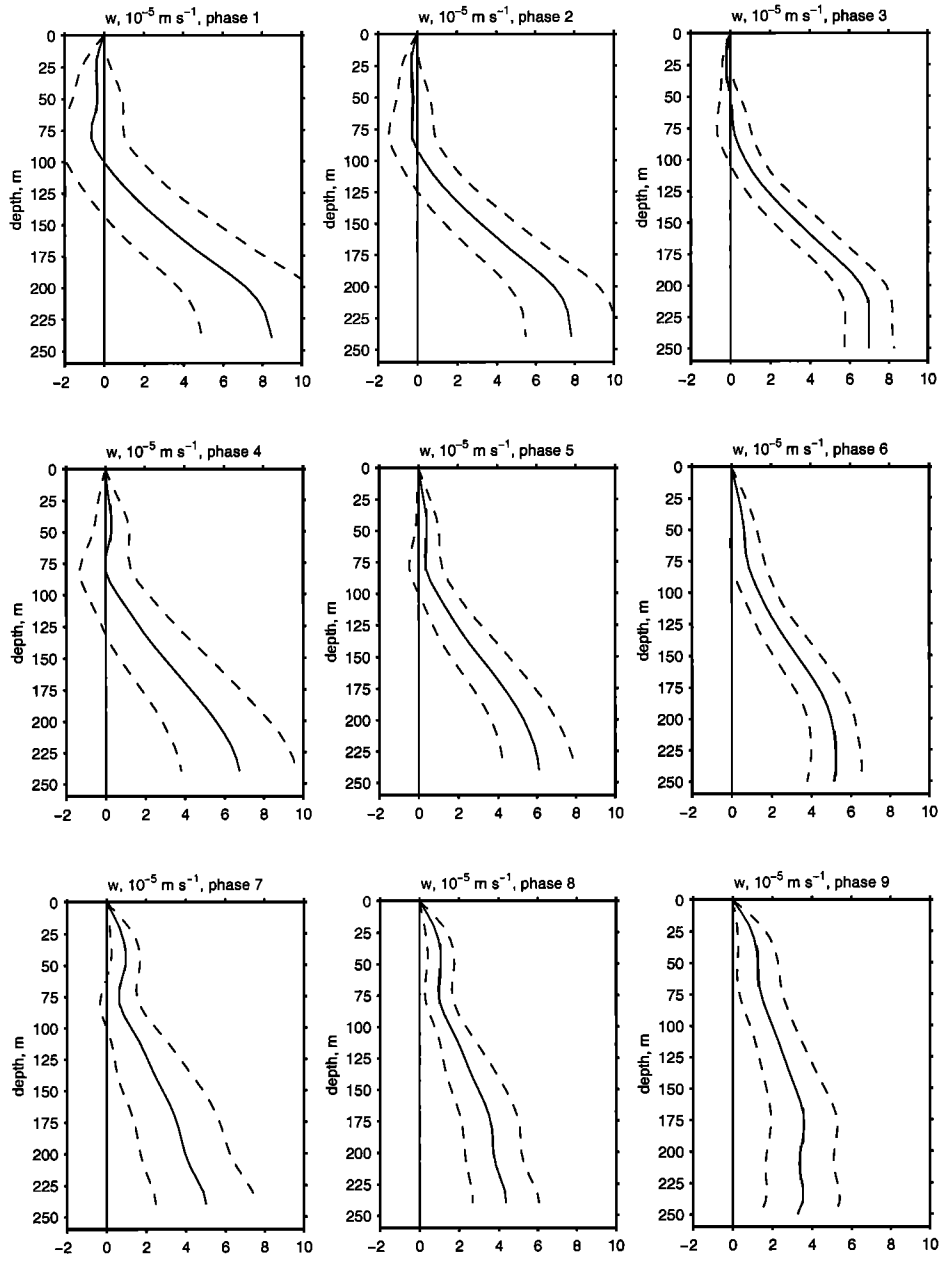

Figure 5. Mean vertical velocity (thick solid line) versus depth for all nine phases of the vertical velocity estimation. The averaging period is March 1, 1992, until February 15, 1993, the units are 10^{-5} m s^{-1}, the dashed lines are plus and minus the standard deviation of the mean, and the phase number of each panel corresponds to the numbering convention used in the text.

of the difference of the squares of constant and constant shear extrapolated near-surface values. The extrapolation error is independent of depth below 30 m, and the resulting error in the phase five w estimation is depicted in Figure 6c.

Error in w due to the extrapolated near-surface values is largest when the horizontal velocity components near the surface (<30 m) have large vertical shear that is not accounted for by the constant extrapolation. During the months of June and October 1992 the u component velocity, near the surface at 0°, 156°E, is strong westward and has large vertical shear. This coincides with periods of large surface extrapolation error (Figure 6c). Extrapolation error seems independent of the vertical structure of the deeper currents brought about by the subsurface westward flow.

Finite difference error occurs because the data are recorded at finite intervals in space and time, requiring that the model equations be discretized as described in section 2.3. Consequently, the spatial curvature of velocity measurements creates a bias in the w estimation. To get an idea as to the magnitude of the effect of the curvature in horizontal velocity, nine w phases were plotted in Figure 4. Gradients in horizontal velocity components are not homogeneous in space; otherwise, the w phases would be identical. Unfortunately, the curvature in the horizontal currents that would produce spatial variance in w is also what causes finite difference error. Consequently, part of the variance between the nine phases is true w asymmetry, and the remainder is due to errors including finite difference error. It is not possible to identify how much of the

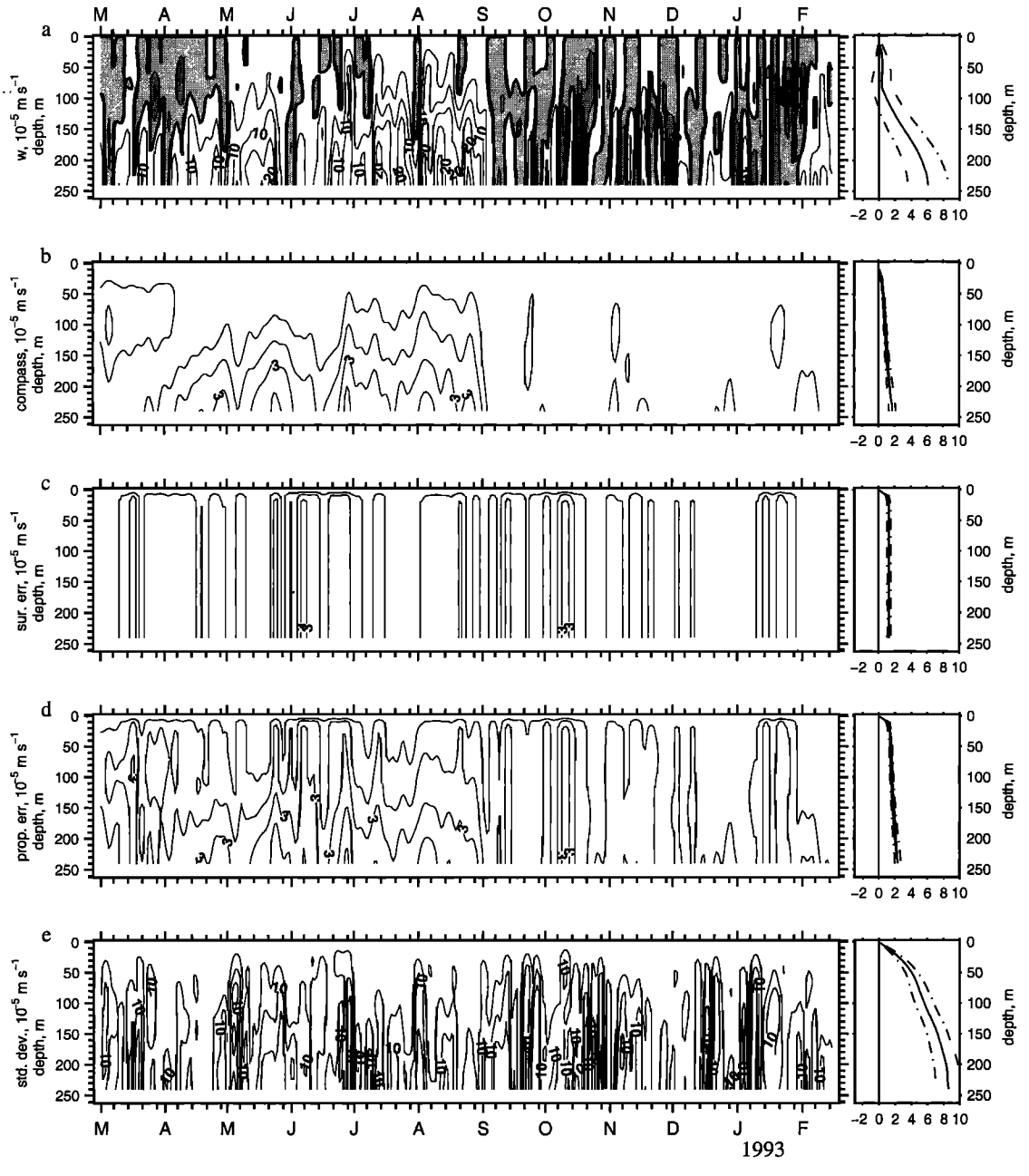

Figure 6. Time-depth contours of (a) vertical velocity phase five, (b) compass calibration error, (c) surface extrapolation error, (d) combined propagation of extrapolation and compass error, and (e) vertical velocity phase variance. Vertical velocity phase standard deviation is computed as the standard deviation of the nine vertical velocity estimates at each depth and time. Propagation of error is used because each error is independent of the other. Units are 10^{-5} m s^{-1}, and the contour interval for Figures 6a and 6e is 5×10^{-5} m s^{-1}, while the contour interval for Figures 6b, 6c, and 6d is 10^{-5} m s^{-1}. To provide error estimates on the timescales of interest, the filter in these data is a 120 hours (5 day) low-pass filter. Using a longer timescale low-pass filter reduces the error.

variance is erroneous. Figure 6e displays the standard deviation of the nine phases at each depth and time. It is reassuring to note that the total standard deviation is not larger than the magnitude of w, suggesting that the error is smaller than w. This is encouraging considering the inherent problems in the w estimate discussed above. Moreover, as will be seen in the following sections, physically identifiable w responses are apparent, indicating that the estimate is robust.

3. Results and Analyses

3.1. First Year, February 1992 Through February 1993

3.1.1. Observed divergence. On average, over the first year of the EMA, above 125 m the u component velocity is convergent, while between 125 and 210 m it is divergent (Figure 7a). Below 210 m, zonal flow is, again, convergent. The zero crossings of $\partial u/\partial x$ correspond to the depth of the sub-

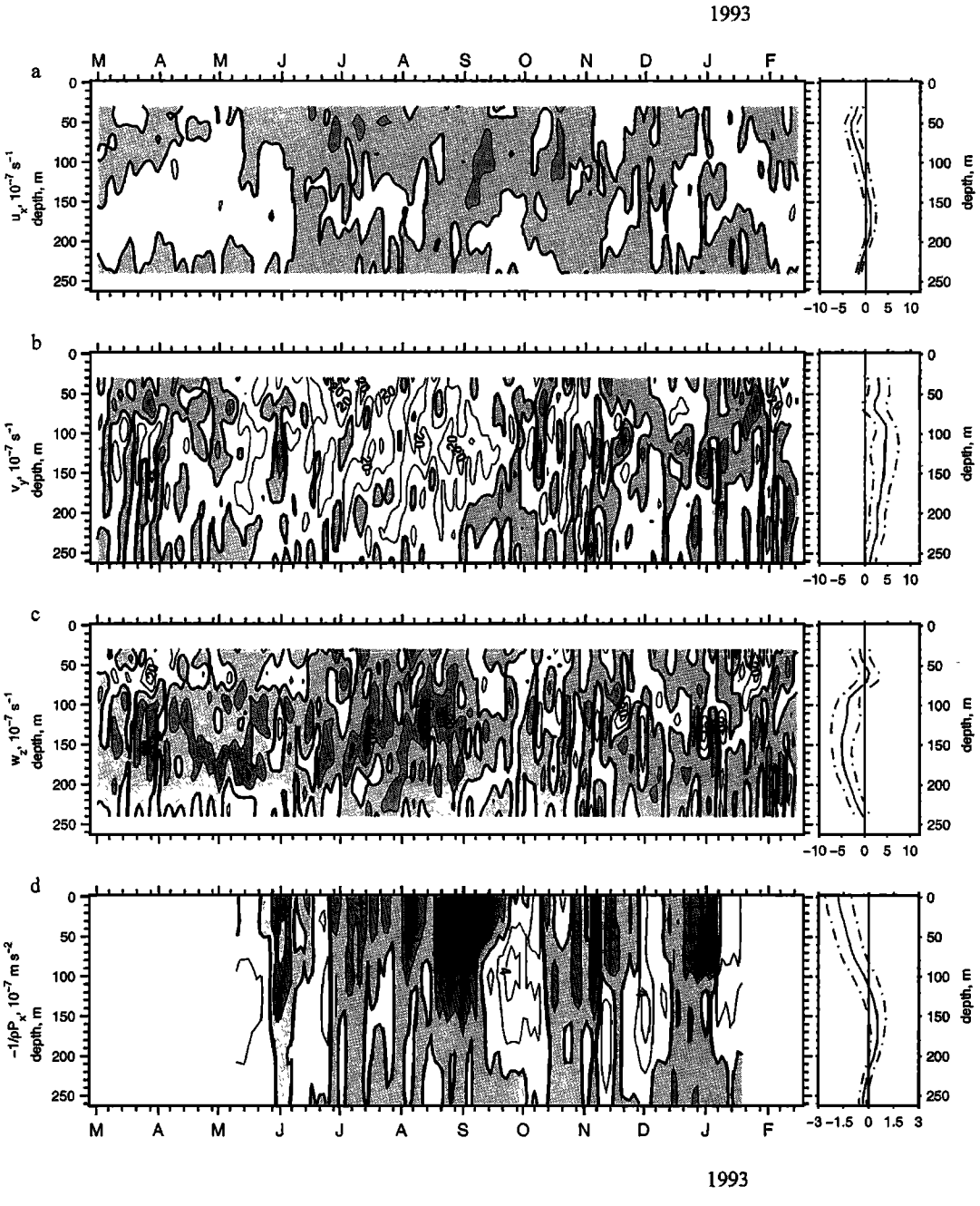

Figure 7. The three terms of the continuity equation, from divergences corresponding to phase five w estimation and zonal pressure gradient, are shown in time-depth contours: (a) zonal divergence $\partial u/\partial x$, (b) meridional divergence $\partial v/\partial y$, (c) vertical divergence $\partial w/\partial z$, and (d) zonal pressure gradient calculated from dynamic height from moorings located at 0°, 160.5°E and 0°, 154°E. The contour interval is 5×10^{-7} s^{-1} for divergence and 2×10^{-7} m s^{-1} for pressure gradient. Divergence and pressure data are filtered to remove oscillations of period <5 days.

surface westward flow (~125 m) and the EUC (~210 m). A similar vertical structure is also found in the zonal pressure gradient (ZPG) force (Figure 7d). The ZPG force, averaged over available data, has the strongest magnitude near the surface and is directed westward ($-1/\rho\ \partial P/\partial x < 0$). Mean ZPG force is directed eastward over the approximate depth range where $\partial u/\partial x$ is positive. These profiles of average $\partial u/\partial x$ and $-1/\rho\ \partial P/\partial x$ are consistent with each other. Near the surface, where the ZPG force tends to decelerate the zonal flow down stream, u is convergent. Conversely, at the depth where the ZPG force tends to accelerate the zonal flow down stream, between ~110 and 220 m, u is divergent.

The v component velocity is divergent, on average, over the upper 250 m (Figure 7b), with a maximum at around 100 m. From geostrophic arguments a negative ZPG force on the equator would result in meridional divergence by producing poleward geostrophic flow just off the equator. Near the surface the mean $\partial v/\partial y$ profile is divergent, and the ZPG force is negative, but at the depth where the ZPG force becomes positive, $\partial v/\partial y$ is still divergent, suggesting that ageostrophic forc-

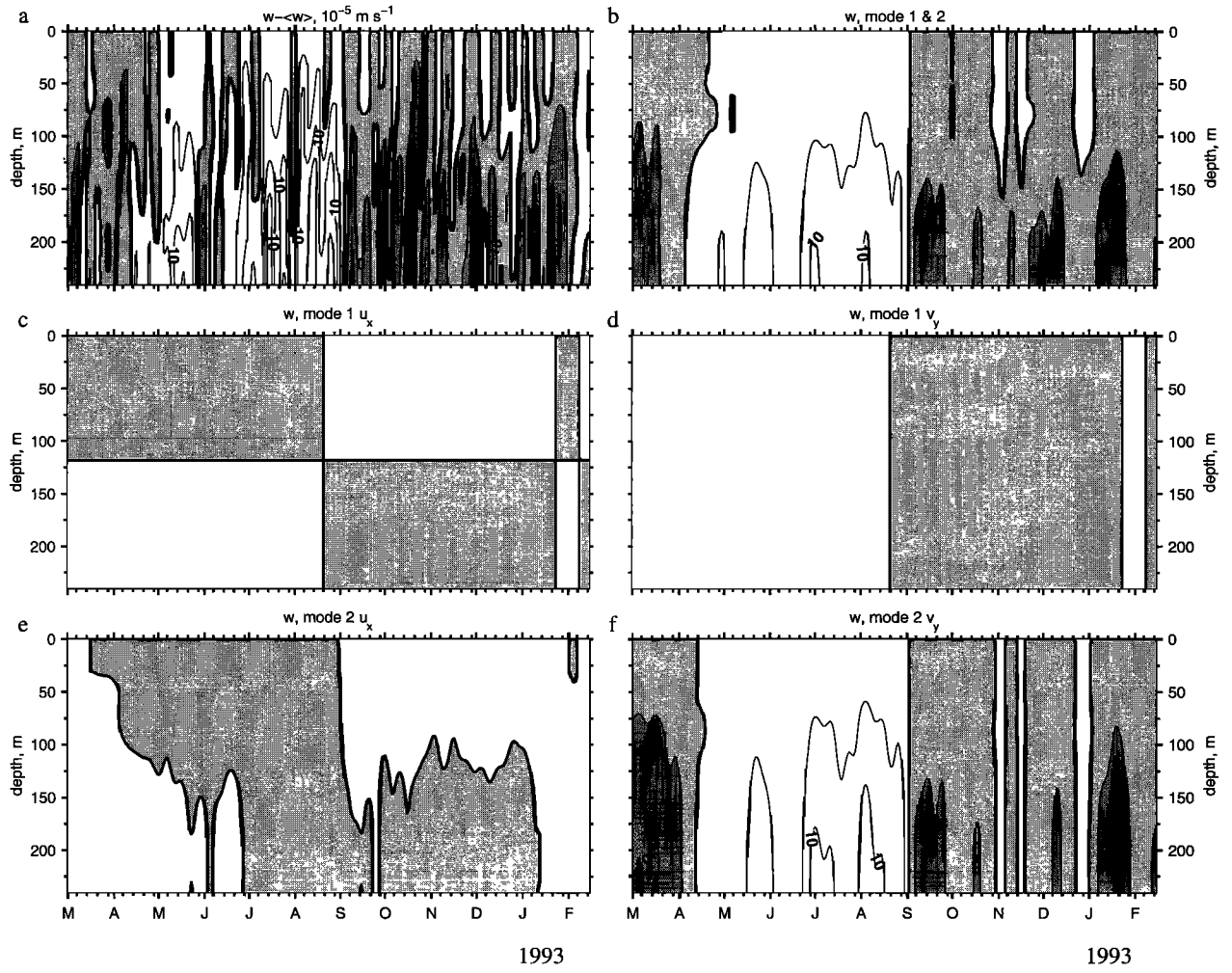

Figure 8. Time domain EOF analysis using ADCP current meter data excluding the surface extrapolation. Time-depth contours of (a) w with the mean removed and (b) w computed from the sum of the first- and second-mode horizontal velocities. Separated into divergence components, w computed from mode one (c) $\partial u/\partial x$ and (d) $\partial v/\partial y$ and w computed from the sum of modes one and two (e) $\partial u/\partial x$ and (f) $\partial v/\partial y$ are shown. The contour interval is 5×10^{-5} m s^{-1} with negative values shaded.

ing is important. Moreover, above 100 m, $\partial v/\partial y$ becomes smaller, in opposition to increased negative ZPG force, suggesting that Ekman convergence due to the westerly winds tends to oppose the geostrophic divergence.

Temporally, when $\partial u/\partial x$ is largely negative (positive), $\partial v/\partial y$ is largely positive (negative). A good example is from June through August 1992 when $\partial u/\partial x$ is negative and $\partial v/\partial y$ is positive (Figures 7a and 7b). This coincides with the strong upwelling and negative ZPG force prior to the onset of the subsurface westward flow and during the deceleration of the EUC (Figures 2, 6a, and 7d). During July, August, and early September, $\partial v/\partial y$ is positive, and the ZPG force is negative. Starting in September, the ZPG force is more variable (with more positive patches), coincident with a more variable $\partial v/\partial y$ (with more negative patches). The measure of how much $\partial u/\partial x$ and $\partial v/\partial y$ fail to cancel is, of course, given by $\partial w/\partial z$ (Figure 7c). During June through August 1992, when horizontal divergence is large, $\partial w/\partial z$ is also large and primarily negative, which results in positive w on average.

3.1.2. Modes of variability. Using empirical orthogonal function (EOF) analysis, we have analyzed the modes of variability inherent in the w estimation. The EOF included the entire set of horizontal velocity components with the means removed, both u and v from 30 to 240 m from all five moorings, filtered to remove oscillations with a period shorter than 8 days. Divergence and vertical velocity were then calculated from the EOF output.

The results indicate that two modes, representing 40 and 24% of the total variance, capture much of the lowest order w variability. Phase five w with the mean removed and the corresponding w computed from the first two modes from the EOF analysis are shown in Figures 8a and 8b. High-frequency variability is not retained in modes one and two.

To identify how the variability is distributed, mode one and the sum of modes one and two were used to compute the contribution of $\partial u/\partial x$ and $\partial v/\partial y$ to the w estimate, separately. Results indicate that little divergence is obtained in the first mode, and thus w computed from first mode $\partial u/\partial x$ and $\partial v/\partial y$ has a magnitude of $<5 \times 10^{-5}$ m s^{-1} (Figure 8). The temporal and vertical structure of the first mode $\partial v/\partial y$ component of w is more consistent with the lowest-order variability of w than is the first mode $\partial u/\partial x$ component of w.

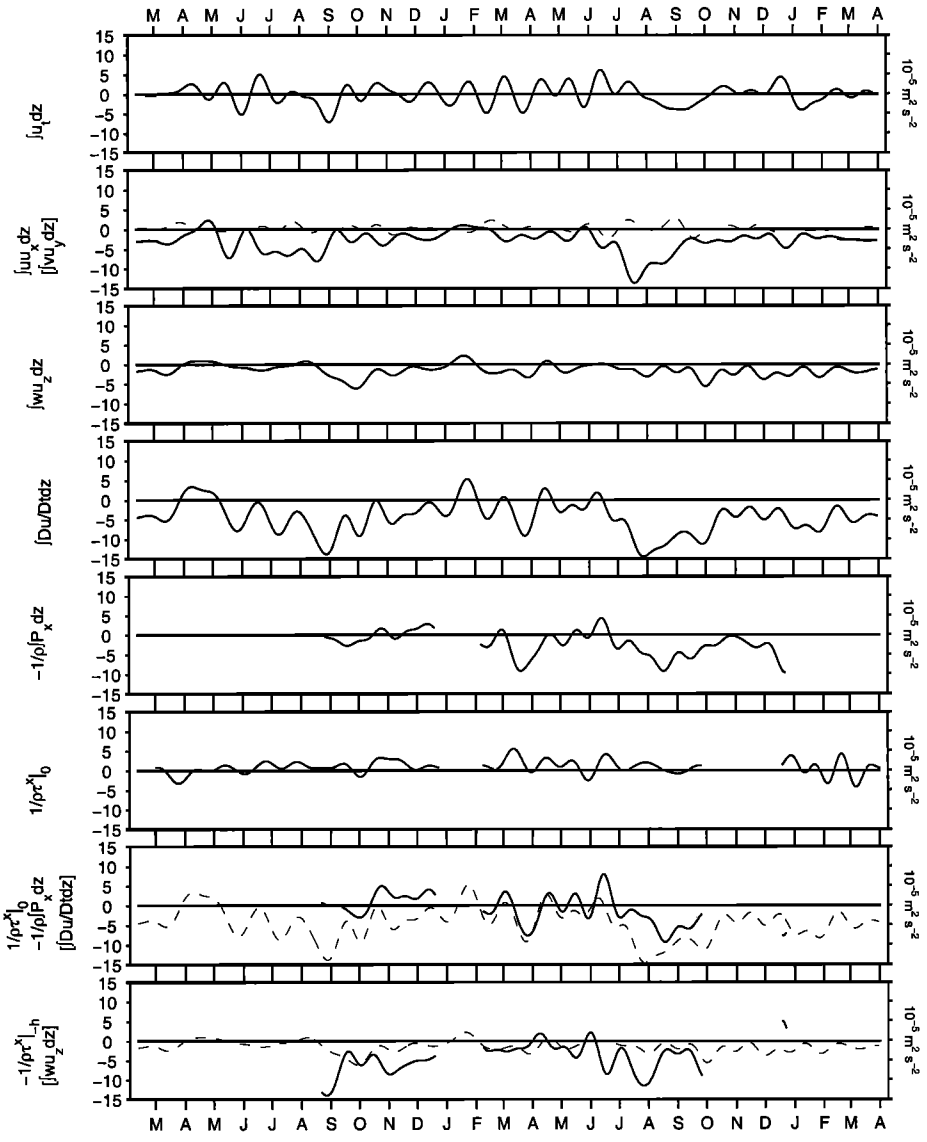

Figure 9. All terms of the zonal momentum balance integrated to 240 m. The terms are indicated to the left of each panel where the terms in brackets correspond to the dashed line. Units are 10^{-5} m^2 s^{-2}.

The largest amount of divergence is found in second mode $\partial v/\partial y$, whereas $\partial u/\partial x$ seems merely to contribute to the vertical structure of w. This result indicates that the variability of w is primarily due to $\partial v/\partial y$, and $\partial u/\partial x$'s contribution is primarily through the mean (Figure 7) since the variability of $\partial u/\partial x$ is less divergent. This suggests that w comes primarily from the resolved low modes. Higher-mode variances (presumably unresolved) make a smaller contribution.

3.2. Both Years, February 1992 Through April 1994

3.2.1. Zonal momentum balance and w. The zonal momentum equation evaluated with in situ zonal pressure gradient, zonal wind stress, and 3-D velocity data provides an independent consistency check for w. *Cronin et al.* [2000], in terms of layered zonal momentum balances using COARE EMA data and the present estimate of w, showed that although the lowest-order dynamics are due to wind stress and zonal pressure gradients, the nonlinear terms can be large. Taking another brief look at this balance, we use the zonal momentum equation integrated with depth to $z = -240$ m:

$$\int_{-240}^{0} \left[\frac{\partial u}{\partial t} + u \frac{\partial u}{\partial x} + v \frac{\partial u}{\partial y} + w \frac{\partial u}{\partial z} \right] dz$$

$$= -\frac{1}{\rho} \int_{-240}^{0} \frac{\partial P}{\partial x} dz + \frac{1}{\rho} (\tau_{x|0} - \tau_{x|-240}). \quad (1)$$

In this treatment, P is pressure, ρ is density, and τ_x is the Reynolds stress where $\tau_{x|0}$ is equal to the surface zonal wind stress and $\tau_{x|-240}$ is the-vertical turbulent stress at 240 m obtained as a residual. The results shown in Figure 9 indicate that vertical advection, which was calculated using the phase five w estimate, agrees in magnitude and temporal variability with pressure and surface wind stress. The seasonality in vertical advection is similar to that of the other terms, showing larger magnitude in the boreal fall after the local deceleration of the EUC. The residual turbulent stress at 240 m also shows a seasonality, indicating heightened mixing during boreal sum-

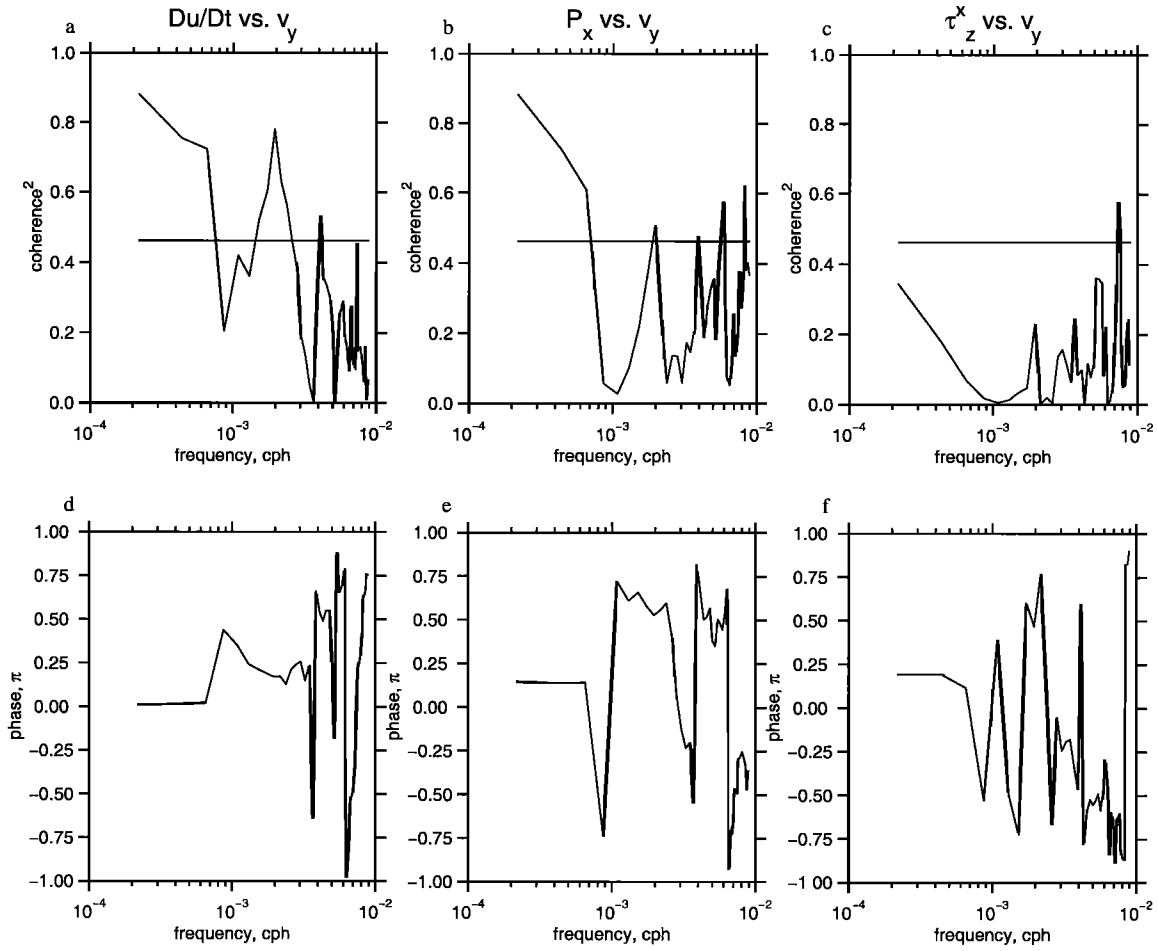

Figure 10. Coherence squared and phase of $\partial v/\partial y$ with (a) and (d) Du/Dt, (b) and (e) $\partial P/\partial x$, and (c) and (f) $\partial \tau_x/\partial z$ versus frequency for the longest continuous period of pressure gradient data, from March 22, 1993, until September 27, 1993. The bandwidth for the calculation is 0.002 cph, resulting in 10 degrees of freedom, and the 90% significance level is 0.4622, indicated by the solid line in Figures 10a, 10b, and 10c. Phase in Figures 10d, 10e, and 10f is in units of π.

mer. These results have motivated a more detailed analysis of momentum by the authors that is presently in preparation.

3.2.2. Components of $\partial v/\partial y$. Evaluation of (1) reveals that the zonal momentum balance on the equator is 3-D, highly frictional, and pressure driven. The magnitude of the acceleration terms suggests that the Earth's rotation will make a negligible contribution in the vicinity of the equator. Nevertheless, geostrophic and Ekman divergences due to the Coriolis force just off the equator will contribute to the dynamics within the inertial boundary layer on the equator. To obtain a quantitative measure of the influence of Ekman and geostrophic dynamics, we use the zonal momentum equation to estimate the divergence of v across the equator. Taking a finite difference of the zonal momentum equation evaluated at a distance y north and south of the equator, we obtain

$$\frac{\Delta v}{\Delta y} \cong \frac{1}{yf}\frac{Du}{Dt} + \frac{1}{yf\rho}\frac{\partial P}{\partial x} - \frac{1}{yf\rho}\frac{\partial}{\partial z}\tau_x, \qquad (2)$$

where f denotes the Coriolis parameter and we have assumed that the material derivative Du/Dt, the zonal pressure gradient $\partial P/\partial x$, and the vertical divergence of zonal stress $(\partial/\partial z)\tau_x$ are uniform across the equator from $-y$ to y. The first term on the right represents the acceleration resulting in meridional divergence, whereas the second and third terms represent geostrophic and Ekman contributions to meridional divergence. Though acceleration and pressure gradient are not likely to be uniform across the equator, (2) identifies the major factors governing meridional divergence.

Coherence analysis reveals that the acceleration and the zonal pressure gradient are coherent at timescales greater than 2 months, but the zonal wind stress is not significantly coherent at the 90% level (Figure 10). This suggests that local Ekman dynamics make only a minor contribution to $\partial v/\partial y$. Coherence with the acceleration term indicates the region is time-dependent and nonlinear, and coherence with pressure suggests that geostrophic dynamics are important to equatorial upwelling. Far field winds, however, are not accounted for in this analysis and may contribute to divergence via the equatorial waveguide and may show up in the acceleration term.

In an attempt to determine the latitude at which geostrophic dynamics are important to the equatorial divergence we have performed a linear least squares regression between integrated zonal pressure gradient force and integrated meridional divergence. The obtained slope is an estimator for $1/yf$, the coefficient in front of the pressure gradient force in (2). The resulting coefficient corresponds to a value of y at $\pm 1.5°$ from the

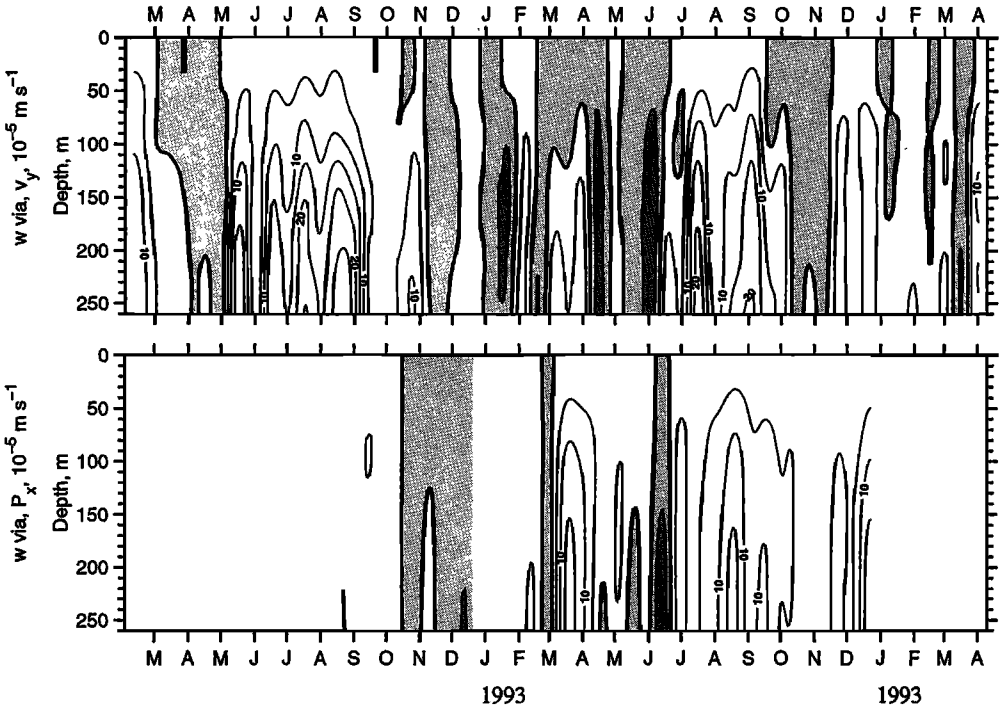

Figure 11. Estimates of w calculated from pressure gradient–derived $\partial v/\partial y$ and from observed $\partial v/\partial y$. Units are in 10^{-5} m s^{-2} with a contour interval of 5×10^{-5} m s^{-2}. Data are filtered to remove oscillations of period 25 days or less.

equator. Using this value of y, we calculate the second term on the right-hand side of (2) as an estimate of the geostrophic $\partial v/\partial y$. Integrating with depth, we obtain an estimate of w resulting solely from geostrophic meridional divergence. For comparison we also integrate the observed $\partial v/\partial y$ to obtain an estimate of w solely from observed meridional divergence. The results show a reasonable agreement between these calculations, indicating that geostrophic dynamics are an important part of the observed w (Figure 11). A caveat of this estimation is that the pressure gradient is not uniform across the equator as is evident from the surface pressure fields from the Pacific reanalysis data. The pressure gradient in the western Pacific is opposite in direction to that in the central and eastern Pacific and is asymmetric near the equator (Figure 1).

3.2.3. Meridional asymmetry. Because of the lack of data at the mooring located at 0°, 154°E after February 1992, there are only three possible phases for the second year of EMA data. The variance of these three estimates, during the second year, is larger than the first but can be accounted for by local forcing. In August 1993 there was a strong northward meridional wind across the equator (Figure 12a, dashed line). The result from surface Ekman divergence was downwelling north of the equator and upwelling to the south (Figures 12b and 12d), a response to local meridional winds first suggested by *Cromwell* [1953]. Similar patterns of asymmetric w can be seen at other times during the record as well. For example, consider the opposite asymmetric response of w to southward wind events in May 1992, April 1993, and February and March 1994. Also, the northward wind in October and November 1992 resulted in asymmetric w. There are events that produce unexpected w responses, suggesting other dynamics are important (for example, June 1992).

Using depth-averaged w and calculating its coherence with meridional wind stress, we obtain more quantitative support for the observed meridional asymmetry in w (Figure 13). Phase three w is coherent with meridional wind stress and is nearly π radians out of phase. Phase nine w is coherent with meridional wind stress and is nearly in phase, while phase six w is not coherent with wind stress. This clear relation between meridional wind stress and asymmetries in w occurs in a region where the local zonal winds are not coherent with w.

4. Discussion and Conclusions

The major finding in this paper is that large equatorial upwelling occurs in the western Pacific warm pool in the presence of westerly winds. The 2 year mean w estimation on the equator at 156°E is near zero from the surface down to 60 m and then grows increasingly positive down to the deepest data at 260 m reaching a value in excess of 3×10^{-5} m s^{-1}. Local zonal winds are primarily westerly during this time period but are not coherent with the w estimation, and downwelling is not found near the surface. Instead, geostrophic divergence counteracts the effect of Ekman convergence, resulting in negligible vertical motion near the surface. This is also found by G. S. E. Lagerloef (personal communication, 2000) using satellite altimetry and wind data. Using techniques developed by *Lagerloef et al.* [1999], both Ekman and geostrophic components of equatorial upwelling are found to cancel, resulting in small vertical motion near the surface in the warm pool.

In contrast, the w profile found in the central Pacific (0°, 140°W) by *Weisberg and Qiao* [2000] exhibits upwelling above the EUC core and downwelling below. The difference is that at 0°, 140°W the ZPG force is eastward, and the easterly trade winds blow consistently. Both Ekman and geostrophic dynamics play an important role. Recent model results also differ

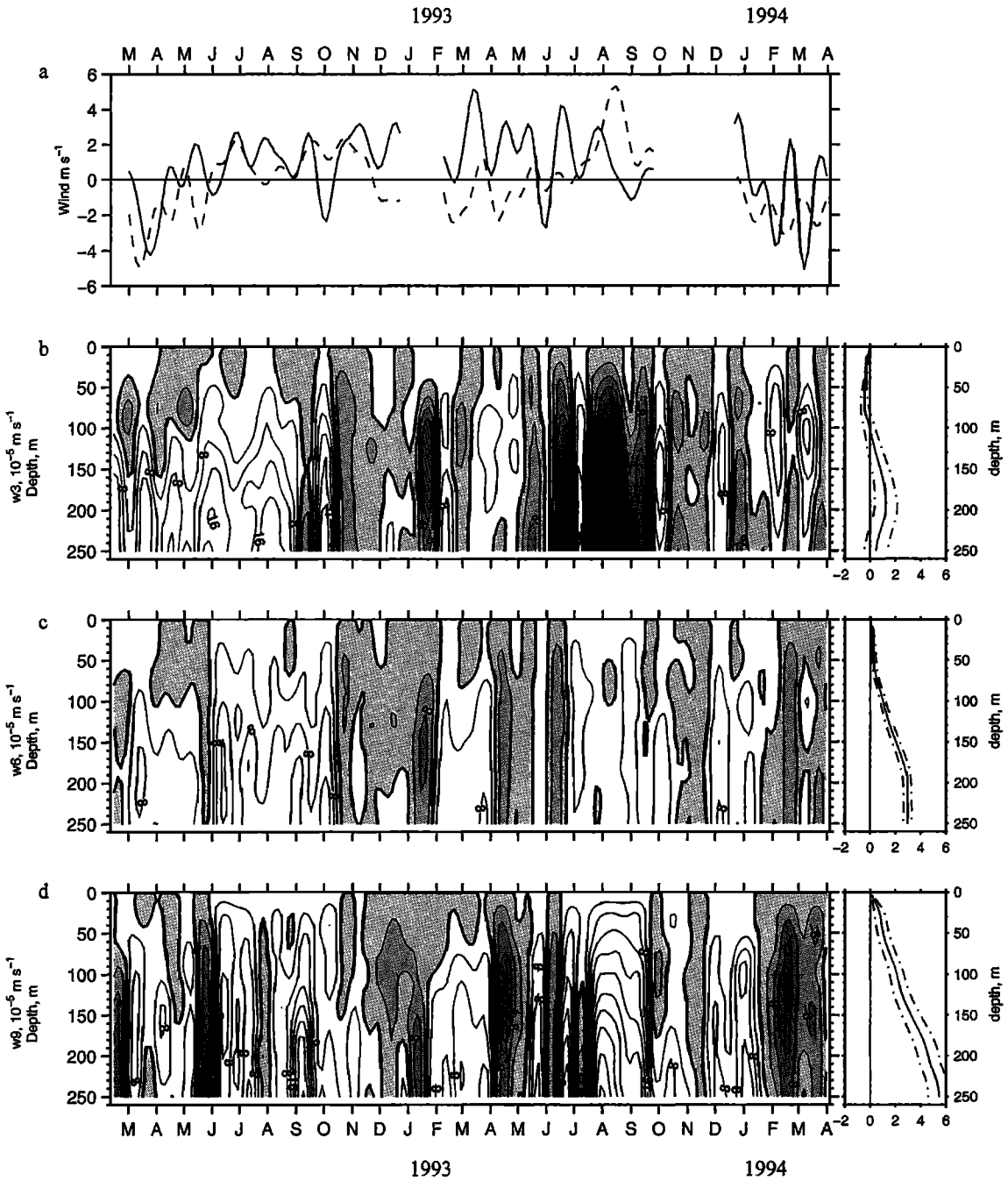

Figure 12. Local winds and phases three, six, and nine of vertical velocity estimation for the time period from February 10, 1992, until April 4, 1994. (a) The zonal (solid) and meridional (dashed) winds are in units of m s^{-1}. The units of vertical velocity (b) phase three, (c) phase six, and (d) phase nine are 10^{-5} m s^{-1}. The panels to the right of the time-depth contours are the corresponding mean depth profile with the associated standard deviation of the mean. Data are filtered to remove oscillations of period 25 days or less.

from the present analysis by producing downwelling in the western Pacific [*Rothstein et al.*, 1998]. This disparity with model results may be due to incomplete model physics as manifested in turbulence parameterization.

Random errors in the w estimation are found to be $<10^{-5}$ m s^{-1}, while systematic errors (finite difference error, systematic instrument error, and error due to the surface extrapolation) may be larger. Although the magnitude of all possible errors cannot be fully obtained, results suggest that the w estimate is larger than the net accumulation of errors.

Upwelling is found to be largest in the boreal summer months when the entire upper water column is flowing eastward after the EUC intensity peaks and begins to decelerate against an adverse ZPG force (Figures 2, 6a, and 7). The zonal momentum balance indicates that turbulent stress is also larger when upwelling is prominent during the boreal summer. Ver-

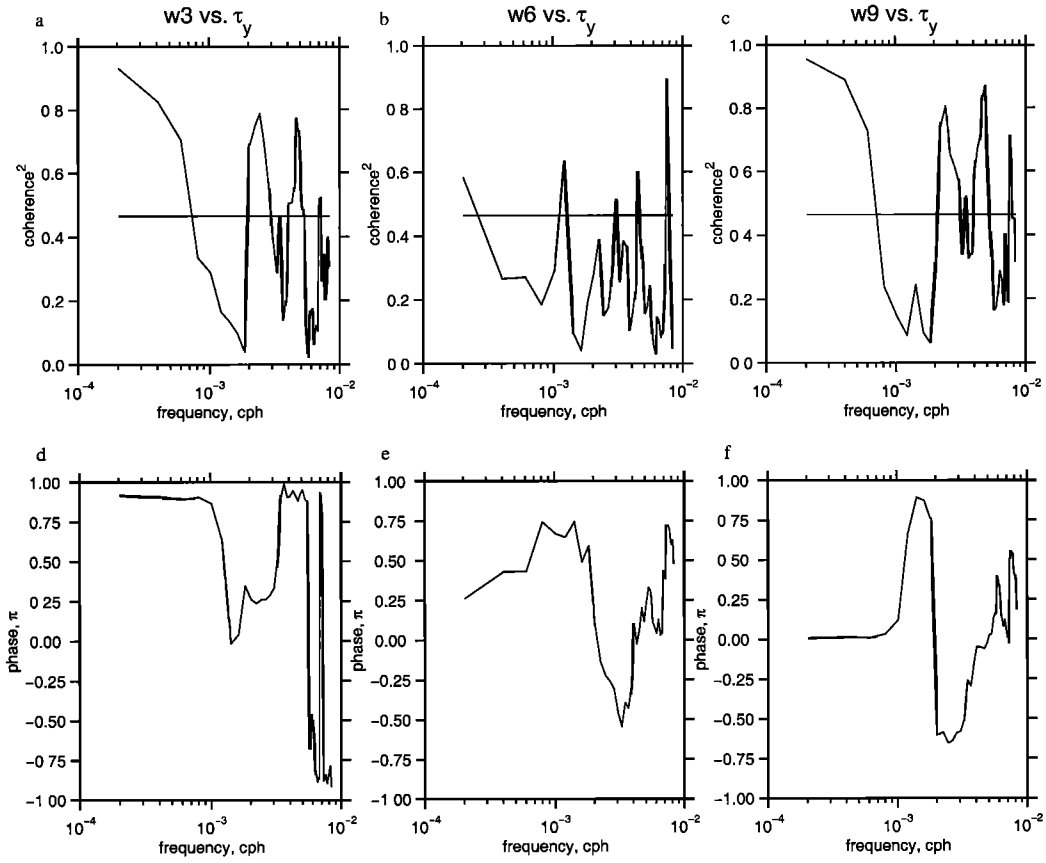

Figure 13. Coherence squared and phase of meridional wind stress τ_y with (a) and (d) w phase 3, (b) and (e) w phase 6, and (c) and (f) w phase 9 versus frequency for the longest continuous period of wind stress data, from March 11, 1993, until September 27, 1993. The bandwidth for the calculation is 0.002 cph, resulting in 10 degrees of freedom, and the 90% significance level is 0.4643, indicated by the solid line in Figures 13a, 13b, and 13c. Phase in Figures 13d, 13e, and 13f is in units of π.

tical velocity becomes variable with extended periods of downwelling after the onset of subsurface westward flow in September. Interannual variability is also observed with larger upwelling during the stronger El Niño in 1992 compared with 1993.

Agreement of the geostrophic w with w computed from observed $\partial v/\partial y$ suggests that the seasonal cycle in upwelling is consistent with the large-scale evolution of the pressure field. The latitude at which the geostrophic term of (2) is most closely linearly related with observed $\partial v/\partial y$ is also consistent with the inertial boundary layer length scale $(u/\beta)^{1/2}$. Using $u = 0.4$ m s^{-1} (Figure 2) and $\beta = 2 \times 10^{-11}$ s^{-1} m^{-1}, we find the boundary scales to be about 1.3° from the equator, which is close the value of 1.5° found in section 3.2.2.

Increased variance between w phases is observed in 1993 relative to 1992 and is attributed to local meridional winds. In August 1993 a strong northward wind event produced downwelling north of the equator and upwelling to the south. Smaller asymmetries in w are also found in response to meridional winds throughout the 2 year record. ZPG variations control the low-frequency variations in w, while local meridional winds produce asymmetry. Local zonal winds are not coherent with w, but large-scale winds result in the pressure gradients observed locally.

In a fully 3-D flow, as found on the equator, vertical advection is an important contributor to the balances of mass, heat, and momentum. Since the role of vertical advection in these balances is tied to mixing [e.g., *Weisberg and Qiao*, 2000], improved observations of equatorial upwelling are necessary for advancing the parameterizations of mixing in coupled ocean-atmosphere models. This has been recognized for the equatorial cold tongue. Here we show similar importance for the warm pool, where seasonal and interannual variations of the zonal pressure gradient give rise to large, relatively deep upwelling. More specifically, designed arrays of velocity profiles, coupled with temperature, salinity, and surface flux measurements, can provide an effective means of diagnosing vertical velocity and the advective contributions to the balances of mass, heat, and momentum.

Acknowledgments. Support for this work was provided by the Ocean Sciences Division, National Science Foundation grant OCE-9525912. The authors thank J. Donovan and R. Cole from the Ocean Circulation Group at USF for their part in the deployment and data editing procedures of the USF ADCP moorings located at 0.75°N, 156°E; 0.75°S, 156°E; and 0°, 157.5°E. We thank M. McPhaden for the TAO array contributions to the EMA, M. Cronin for the dynamic height data from TAO and EMA moorings, and K. Kutsuwada for the 0°, 154°E ADCP mooring data. Leetmaa Pacific Ocean Reanalysis was provided by the NOAA-CIRES Climate Diagnostics Center, Boulder, Colorado, from their Web site at http://www.cdc.noaa.gov/.

References

Beers, Y., *Introduction to the Theory of Error*, Addison-Wesley-Longman, Reading, Mass., 1957.

Bryden, H. L., and E. C. Brady, Diagnostic model of the three-dimensional circulation in the upper equatorial Pacific Ocean, *J. Phys. Oceanogr., 15*, 1255–1273, 1985.

Bubnov, V., Vertical motions in the central equatorial Pacific, *Oceanal. Acta, Proc. Int. Symp. Equatorial Vertical Motion*, 15–17, 1987.

Chatfield, C., *Statistics for Technology*, Chapman and Hall, New York, 1978.

Cromwell, T., Circulation in a meridional plane in the central equatorial Pacific, *J. Mar. Res., 12*, 196–213, 1953.

Cronin, M. F., and M. J. McPhaden, The upper ocean heat balance in the western equatorial Pacific warm pool during September–December 1992, *J. Geophys. Res., 102*, 8533–8553, 1997.

Cronin, M. F., M. J. McPhaden, and R. H. Weisberg, Wind-forced reversing jets in the western equatorial Pacific, *J. Phys. Oceanogr., 30*, 657–676, 2000.

Godfrey, J. S., R. A. Houze Jr., R. H. Johnson, R. Lukas, J.-L. Redelsperger, A. Sumi, and R. Weller, Coupled Ocean-Atmospheric Response Experiment (COARE): An interim report, *J. Geophys. Res., 103*, 14,395–14,450, 1998.

Halpern, D., and P. H. Freitag, Vertical motion in the upper ocean of the equatorial eastern Pacific, *Oceanal. Acta, Proc. Int. Symp. Equatorial Vertical Motion*, 19–26, 1987.

Halpern, D., R. A. Knox, D. S. Luther, and S. G. H. Philander, Estimates of equatorial upwelling between 140°W and 110°W during 1984, *J. Geophys. Res., 94*, 8018–8020, 1989.

Helber, R. W., and R. H. Weisberg, Equatorial upwelling in the western Pacific warm pool, in *COARE98 Proceedings of a Conference on the TOGA Coupled Ocean-Atmosphere Response Experiment (Boulder, CO, USA 7–14 July 1998), WMO/TD 940*, World Meteorol. Org., Geneva, 1998.

Johnson, E. S., and D. S. Luther, Mean zonal momentum balance in the upper and central equatorial Pacific Ocean, *J. Geophys. Res., 99*, 7689–7705, 1994.

Kutsuwada, K., and H. Inaba, Year-long measurements of upper-ocea currents in the western equatorial Pacific by acoustic Doppler current profilers, *J. Meteorol. Soc. Jpn., 73*, 665–675, 1995.

Lagerloef, G. S. E., G. T. Mitchum, R. B. Lukas, and P. P. Niiler, Tropical Pacific near-surface currents estimated from altimeter, wind, and drifter data, *J. Geophys. Res., 104*, 23,313–23,326, 1999.

Leetmaa, A., and M. Ji, Operational hindcasting of the tropical Pacific, *Dyn. Atmos. Oceans, 13*, 465–490, 1989.

Parratt, L. G., *Probability and Experimental Errors in Science*, John Wiley, New York, 1961.

Qiao, L., and R. H. Weisberg, Zonal momentum balance of the equatorial undercurrent in the central Pacific, *J. Phys. Oceanogr., 27*, 1094–1119, 1997.

Rothstein, L. M., R.-H. Zhang, A. J. Busalacchi, and D. Chen, A numerical simulation of the mean water pathways in the subtropical and tropical Pacific Ocean, *J. Phys. Oceanogr., 28*, 322–343, 1998.

Weingartner, T. J., and R. H. Weisberg, On the annual cycle of equatorial upwelling in the central Atlantic Ocean, *J. Phys. Oceanogr., 21*, 68–82, 1991.

Weisberg, R. H., and L. Qiao, Equatorial upwelling in the central Pacific estimated from moored velocity profiles, *J. Phys. Oceanogr., 30*, 105–124, 2000.

Weisberg, R. H., J. C. Donovan, and R. D. Cole, The Coupled Ocean-Atmosphere Response Experiment (COARE) equatorial array: A report on data collected using subsurface moored acoustic Doppler current profilers, February 1992–March 1993, Univ. of South Fla., St. Petersburg, 1993.

Weisberg, R. H., J. C. Donovan, and R. D. Cole, The Coupled Ocean-Atmosphere Response Experiment (COARE) equatorial array: A report on data collected using subsurface moored acoustic Doppler current profilers, March 1993–April 1994, Univ. of South Fla., St. Petersburg, 1994.

Wyrtki, K., An estimate of equatorial upwelling in the Pacific, *J. Phys. Oceanogr., 11*, 1205–1214, 1981.

Wyrtki, K., and B. Kilonsky, Mean water and current structure during the Hawaii-to-Tahiti Shuttle Experiment, *J. Phys. Oceanogr., 14*, 242–254, 1984.

R. W. Helber and R. H. Weisberg, Department of Marine Science, University of South Florida, 140 7th Avenue South, St. Petersburg, FL 33701-5506. (helber@marine.usf.edu)

(Received May 1, 2000; revised November 21, 2000; accepted January 12, 2001.)